How to fragment peralkaline rhyolites: Observations on pumice using combined multi-scale 2D and 3D imaging

Ery C. Hughes [a,b,*], David A. Neave [a,c], Katherine J. Dobson [d,e], Philip J. Withers [f], Marie Edmonds [a]

[a] Department of Earth Sciences, University of Cambridge, Cambridge CB2 3EQ, UK
[b] School of Earth Sciences, University of Bristol, Bristol BS8 1RJ, UK
[c] Leibniz Universität Hannover, Institut für Mineralogie, 30167 Hannover, Germany
[d] Department of Earth and Environmental Sciences, Ludwig-Maximilians Universität München, 80333 München, Germany
[e] Department of Earth Sciences, Durham University, Durham DH1 3LE, UK
[f] Manchester X-ray Imaging Facility, School of Materials, University of Manchester, Manchester M13 9PL, UK

ARTICLE INFO

ABSTRACT

Peralkaline rhyolites are volatile-rich magmas that typically erupt in continental rift settings. The high alkali and halogen content of these magmas results in viscosities two to three orders of magnitude lower than in calc-alkaline rhyolites. Unless extensive microlite crystallisation occurs, the calculated strain rates required for fragmentation are unrealistically high, yet peralkaline pumices from explosive eruptions of varying scales are commonly microlite-free. Here we present a combined 2D scanning electron microscopy and 3D X-ray microtomography study of peralkaline rhyolite vesicle textures designed to investigate fragmentation processes. Microlite-free peralkaline pumice textures from Pantelleria, Italy, strongly resemble those from calc-alkaline rhyolites on both macro and micro scales. These textures imply that the pumices fragmented in a brittle fashion and that their peralkaline chemistry had little direct effect on textural evolution during bubble nucleation and growth. We suggest that the observed pumice textures evolved in response to high decompression rates and that peralkaline rhyolite magmas can fragment when strain localisation and high bubble overpressures develop during rapid ascent.

© 2017 The Authors. Published by Elsevier B.V. This is an open access article under the CC BY license (http://creativecommons.org/licenses/by/4.0/).

1. Introduction

Peralkaline rhyolites, although less common than their calc-alkaline counterparts, are nonetheless found in many settings including continental rifts, ocean islands and back-arc basins. During the Holocene, central volcanoes along the East African Rift, from Afar to Tanzania, have produced explosive ignimbrite-forming eruptions of peralkaline magma (Macdonald et al., 1987). Today, these volcanic centres threaten many hundreds of thousands of people, yet the dynamics of peralkaline eruptions are poorly understood and have never been observed directly. Despite their high silica contents, peralkaline melts have a relatively low viscosity (equivalent to calc-alkaline andesite for similar water contents) as a result of their alkali-rich nature (molar $(Na_2O + K_2O) / Al_2O_3 > 1$, e.g., Dingwell et al., 1998; Di Genova et al., 2013). Their volatile-free viscosity is two to three orders of magnitude lower than that of calc-alkaline rhyolites: $\sim 10^8$ Pa·s for calc-alkaline rhyolite using the model of Giordano et al. (2008) versus $\sim 10^{5.5}$ Pa·s

for peralkaline rhyolite using the model of Di Genova et al. (2013), both at 1223 K. Peralkaline rhyolite viscosities are so low that the fragmentation threshold for brittle failure (10^8 to 10^9 Pa·s; Papale, 1999) should never be reached during magma ascent and degassing unless significant microlite crystallisation takes place (Di Genova et al., 2013), though numerical modelling has suggested that initial temperature may also exert a strong control on the depth of brittle fragmentation and whether it can occur at all (Campagnola et al., 2016).

Peralkaline magmas are associated with a large range of eruption styles (Houghton et al., 1985a, 1985b, 1987, 1992; Mahood and Hildreth, 1986; Stevenson and Wilson, 1997). For example, on the island of Pantelleria, Italy, magmas with near-identical major element compositions have produced domes, lava flows (including fountain-fed agglutinates), pumice cones, thick tephra fall deposits and pyroclastic flow deposits (Villari, 1974; Mahood and Hildreth, 1986; Civetta et al., 1988, 1998; Stevenson and Wilson, 1997; White et al., 2009; Neave et al., 2012; Williams et al., 2013). The widespread welding and rheomorphism of the ignimbrites and fall deposits (Schmincke, 1974; Wolff and Wright, 1981; Mahood, 1984) are a consequence of the low viscosity and correspondingly low glass transition temperature (T_g) of peralkaline melts, which can allow deformation to continue for many days after emplacement (Di Genova et al., 2013).

* Corresponding author at: School of Earth Sciences, University of Bristol, Bristol BS8 1RJ, UK.
E-mail address: ery.hughes@bristol.ac.uk (E.C. Hughes).

In this study, we use textural observations made on pumices from Pantelleria, Italy, to investigate the mechanisms of peralkaline rhyolite fragmentation. Our aim is to unravel the vesiculation and crystallisation processes in operation during magma ascent and hence understand magma properties to the point of fragmentation. Vesicle textures preserve information about bubble nucleation and growth, but are also modified by deformation, coalescence and outgassing (e.g., Sparks, 1978; Klug and Cashman, 1994; Sable et al., 2006). A crucial assumption made when interpreting pyroclast vesicle textures is that they represent the magma at the moment of fragmentation; that they have experienced no post-fragmentation modification (e.g., Houghton and Wilson, 1989). This assumption is valid when samples are rapidly quenched, as is the case for many pumices from Pantelleria, but the timescale over which textural modification occurs depends on magma viscosity, magma composition and the depth of fragmentation (Gurioli et al., 2015).

In order to examine vesicle and crystal textures, as well as their interrelationships, in detail, we combined the complementary methods of multiscale 3D X-ray microtomography (XMT) and high resolution 2D scanning electron microscopy (SEM) (e.g., Gurioli et al., 2008; Giachetti et al., 2011). By integrating these techniques, we obtained high spatial resolution information about the geometry of objects in three dimensions, which is critical for understanding eruption processes (Baker et al., 2012). We compare our data to published textural studies of explosive eruptions, and assess similarities and differences in textures, bulk porosities, vesicle population characteristics and strain localisation features. By integrating textural and geochemical data, we reconstruct the peralkaline fragmentation process that accompanies the eruptions of these magmas, and test the limits of existing models to explain magma fragmentation. Finally, we use a fragmentation model to explore the role of overpressure inside rapidly growing bubbles as a driver for strain rate-driven fragmentation during rapid ascent.

2. Geological setting

The Quaternary volcano of Pantelleria (Fig. 1) lies on the thinned continental crust of the E-W extending Sicily Channel (Civile et al., 2008, 2010), and has been active for at least 324 ka (Mahood and Hildreth, 1986). The mafic northwest portion of the island is separated from the caldera-dominated, felsic southwest portion by N-S striking regional faults (Catalano et al., 2009). The volcanic history of Pantelleria has been punctuated by ignimbrite-forming eruptions (Jordan et al., 2013; Rotolo et al., 2013), of which the ~45.7 ka Green Tuff eruption was the most recent (Villari, 1974; Mahood and Hildreth, 1986; Scaillet et al., 2013). Continuous geochemical zonation in the Green Tuff deposit, from pantellerite (Fe-rich peralkaline rhyolite) at its base to trachyte at its top, may represent the evacuation of a stratified reservoir of cogenetic magmas (Civetta et al., 1988; Williams et al., 2013). Indeed, pantellerites are most likely formed by 70–80% fractional crystallisation of trachytic liquids (White et al., 2009; Neave et al., 2012; Landi and Rotolo, 2015). Small eruptions generating non-welded fall deposits have been most common over the last 20 ka on Pantelleria (Mahood and Hildreth, 1986; Orsi et al., 1991; Scaillet et al., 2013). Deposits from these eruptions have been classed Strombolian from the limited, circular extent of their tephra dispersal (Orsi et al., 1991, 1989; Stevenson and Wilson, 1997; Rotolo et al., 2007), in line with similar observations from Mayor Island, New Zealand (Houghton et al., 1985a).

Cuddia di Mida is the site of one such Strombolian eruption, which produced a small pumice cone around the eruptive vent (Fig. 1; Orsi et al., 1991). Deposits from the Cuddia di Mida eruption are characteristic of the numerous small explosive eruptions that have taken place since the ~45.7 ka Green Tuff eruption, making it well suited to a study of the eruption dynamics and fragmentation of peralkaline magmas. The lowermost layer of the sequence is an explosion breccia
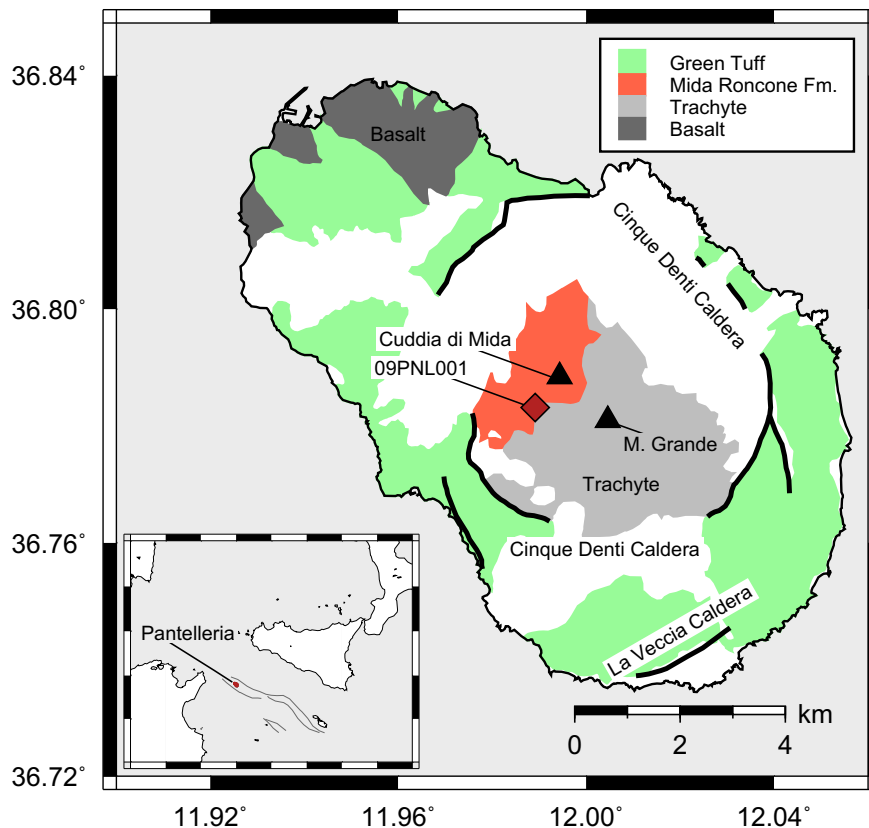

Fig. 1. Geological map of Pantelleria, Italy, with the location of the sample from Cuddia di Mida (09PNL001) indicated by the red diamond (after Mahood and Hildreth, 1986).

(1 m thick) and is overlain by a poorly-sorted fallout layer, which has an increasing ash content towards the top (0.3 m). Above this is an ashy bed (0.08 m) overlain by a much thicker, massive, poorly-sorted fall deposit (1.2 m) (Orsi et al., 1991). The Cuddia di Mida deposits have not been dated, but the eruption probably occurred at a similar time to the Cuddia del Gallo eruption (7.1 ($\pm$0.8) ka; Scaillet et al., 2013): a likely eruption window of 9.7 ($\pm$0.6)–7.1 ($\pm$0.8) ka can be inferred from the ages of the nearby Serra Fastuca and Cuddia del Gallo eruptions (Rotolo et al., 2007; Scaillet et al., 2013). A bulk sample of pumice clasts was collected from a single horizon in the middle of the upper massive layer (Orsi et al., 1991) on the Cuddia di Mida cone (36.781°N, 11.993°E). The unit consists of juvenile clasts ~1–10 cm in diameter (Fig. 2). Grey clasts make up ~95 vol.%, with the remainder made up of black and mixed clasts and non-juvenile clasts which are <10 cm in diameter (obsidians, lithics and occasional enclaves). This is sample number 09PNL001 from Neave et al. (2012).

3. Methods

Density measurements of juvenile material were carried out using the method of Houghton and Wilson (1989), with the type of material (black, mixed or grey pumice) being noted. Bulk densities were converted to porosities using a glass density of 2520 kg·m^{-3}, calculated from the Cuddia di Mida glass composition of Neave et al. (2012) at room temperature and pressure (Bottinga and Weill, 1970; Lange and Carmichael, 1990; Lange, 1997; Toplis et al., 1994; Ochs and Lange, 1999). The grey and black pumices have indistinguishable major element glass compositions and the same glass density was therefore used for both pumice types (Table 1). Grey pumices exhibit the lowest density of any juvenile material from the Cuddia di Mida eruption. In Strombolian eruptions, grey pumices are thought to represent the films that encase gas slugs and are therefore most likely to capture the moment of fragmentation (Lautze and Houghton, 2005). The black and mixed pumices appear to be collapsed grey pumices and therefore were not considered further as they are unlikely to capture the moment of fragmentation. Cylinders ~10 mm in diameter and ~10–20 mm in height were cut from four clasts (A–D) of the grey pumices for qualitative textural analysis by SEM (Back Scatter Electron mode) and XMT imaging (e.g., A_{10} in Table 2). Two additional cylinders ~5 mm in diameter were cut from clasts A and C (e.g., A_5) in order to acquire high quality XMT images at a range of resolutions. These two cylinders were also imaged by SEM. Full details of SEM and XMT image acquisition and processing, including the calculation of vesicle size distributions which followed the principles employed in the FOAMS software (Shea et al., 2010), are included in Supplementary material 1. All images, both SEM and XMT, are available from the authors upon request.

4. Results

4.1. Porosity

As the histogram of porosities (Fig. 3) shows a bimodal distribution, a robust estimate of the average density of the whole population cannot be made owing to insufficient measurements (67 measurements of juvenile material, of which 48 were grey pumices and 19 were black/mixed pumices) (Bernard et al., 2015). The broad, low porosity mode (mean 36.9 $\pm$ 12.2 vol.%, equivalent density 1.59 $\pm$ 0.31 g·cm^{-3}) consists of black and mixed pumices whereas the narrow, high porosity mode (mean 78.5 $\pm$ 2.7 vol.%, equivalent density 0.54 $\pm$ 0.07 g·cm^{-3}) consists exclusively of grey pumices. Sufficient measurements of the high porosity mode were made to obtain a robust estimate of its average (Bernard et al., 2015). The clasts used for textural analysis are all grey pumices from the high porosity mode. The average porosity estimated from the bulk density of A and C is 76.2 vol.%, which compares well with the vesicularity calculated from 2D SEM images (78.2 vol.%).

4.2. Crystals

Crystal phases are dominantly anorthoclase and aegirine augite (tabular euhedral to angular and broken), alongside subordinate Fe-Ti oxides (generally equant) and aenigmatite (elongate bladed) (Neave et al., 2012). The average crystal content estimated using XMT images (A and C) is 3.24 vol.% (13.7 vol.% when recalculated on a vesicle-free basis) and the average aspect ratio of the crystals is 2.41. Crystal size distributions were not calculated from SEM or XMT images due to the low number of crystals present, i.e., crystal populations are not statistically robust. Therefore, only crystal area contents were measured in SEM images for calculation of crystal-free vesicle number densities. No microlites were observed, even in the highest resolution SEM images (Fig. 4). The uniform BSE intensity of the pumice glasses implies that any nanolites present must be <0.02 μm^2 (<1 pixel on the highest resolution SEM images).

4.3. Qualitative textural analysis of vesicles

Grey pumices (A–D) show a variety of vesicle textures in both SEM and XMT images (Figs. 5–7). In some regions, there is a sub-spherical, unimodal, isotropic vesicle population connected by thin melt films (~10^{-3} mm) that have an overall appearance resembling a polyhedral foam (Fig. 5a). Some regions contain elongate vesicles which have thicker vesicle walls (~10^{-2} mm) than the surrounding regions and therefore appear denser (Fig. 5b). Whilst vesicles within these regions are strongly aligned, nearby regions have different alignments and there is no overall bulk preferred orientation. Medium-sized vesicles
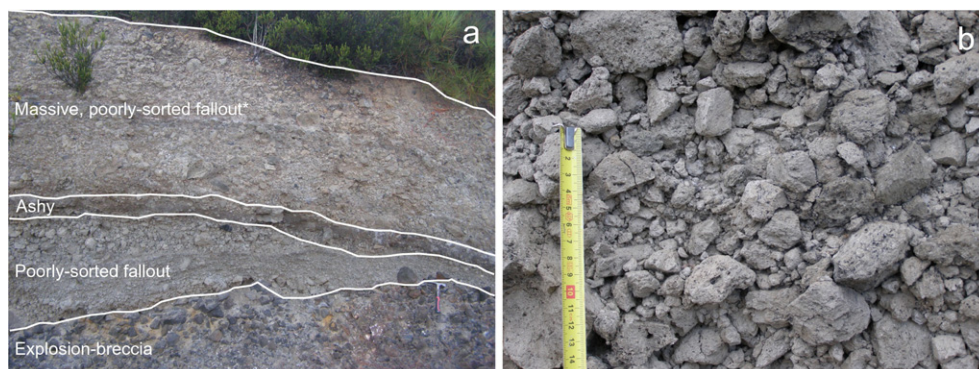

Fig. 2. Photograph of the Cuddia di Mida deposit (a) (lower contact of the explosion-breccia is not visible), where * indicates the layer sampled which is shown in detail (b).

Table 1
Major element glass composition in wt.% from Neave et al. (2012) for grey and black pumices from Cuddia di Mida. 1σ errors are shown.

	SiO$_2$	TiO$_2$	Al$_2$O$_3$	FeO	MnO	MgO	CaO	Na$_2$O	K$_2$O	P$_2$O$_5$
Grey	70.74 ± 0.35	0.25 ± 0.02	7.18 ± 0.06	8.73 ± 0.14	0.36 ± 0.01	0.04 ± 0.02	0.34 ± 0.03	6.83 ± 0.07	4.44 ± 0.07	0.01 ± 0.00
Black	70.92 ± 0.27	0.26 ± 0.03	7.14 ± 0.09	8.69 ± 0.20	0.37 ± 0.02	0.04 ± 0.02	0.34 ± 0.03	6.88 ± 0.09	4.49 ± 0.08	0.01 ± 0.00

($L \sim 10^{-1}$ mm, where L is the equivalent diameter of a sphere with the same volume as the vesicle) associated with crystals are often somewhat elongated perpendicular to crystal faces and are connected to the crystals by thin melt films; the crystals themselves are often mantled by melt films (Fig. 5c). The largest vesicles ($L \sim 10^{0}$ mm) are distributed randomly throughout the samples and have highly convoluted surfaces that are often, but not always, associated with crystals or regions of small vesicles (Fig. 5d). The films separating these large vesicles are very thin and often pinch out in the middle to widths thinner than the resolution of the SEM images (0.15 μm). In SEM and XMT images, all samples display all these textures in approximately similar amounts (Figs. 6 and 7) with two exceptions: in SEM images, A$_5$ only displays the polyhedral foam texture with occasional larger vesicles (Fig. 6); and in XMT images, C$_5$ displays more of the elongate and orientated deformation vesicles (Fig. 7).

4.4. Quantitative textural analysis of vesicles

Vesicle size varies by three orders of magnitude in clasts A and C with L ranging from 1.69×10^{-3} mm (SEM; Fig. 6) to 4×10^{0} mm (XMT; Fig. 7). Vesicle wall thicknesses vary from below the resolution of SEM images (<0.15 μm) to ~30 μm (Figs. 5–7). A$_{10}$ and C$_{10}$ contain equal proportions of circular and elongate vesicles (where elongate vesicles are defined as having long axis to short axis ratios > 2) whereas A$_5$ contains 33% elongate vesicles and C$_5$ 62%, as observed qualitatively (Table 2, Figs. 6 and 7). Relationships between the number of vesicles per unit volume (N$_V$) and L from the SEM data are similar for both clasts in the range L = 0.15–4000 μm, with greater variation found at the upper and lower limits of L (Fig. 8a). Stereological correction procedures from Sahagian and Proussevitch (1998) and Mangan et al. (1993) (abbreviated to SP98 and MCN93 respectively throughout), produced similar results (e.g., for A$_{10}$ N$_{V,tot}$ is 7.26×10^{5} mm^{-3} using MCN93 and 6.14×10^{5} mm^{-3} using SP98). Vesicle properties calculated with the more widely used SP98 procedure were carried forward into further calculations (Table 2; Fig. 8a). The XMT data show very similar trends for clasts A and C (Fig. 8b), with greater inter-sample variation for large vesicles (L > 1 mm). In these samples, the XMT data extend the range of L to values half an order of magnitude greater than those recovered by SEM, and the higher number of vesicles observed at larger L means less scattered data at larger vesicle sizes (Fig. 8c). At intermediate values of L ($6 \times 10^{-2} < L < 4 \times 10^{-1}$ mm), XMT and SEM data have very similar N$_V$ distributions (Fig. 8c).

For cumulative vesicle number density (N$_V$ > L), changes in slope at ~2×10^{-2} mm (from SEM data) and ~5×10^{-1} mm (from XMT data) define three segments, which can be fitted with power-law curves (e.g., Blower et al., 2001) (Table 3; Fig. 8d). At small values of L (SEM; L < 2×10^{-2} mm), the curve can be fitted with a power law exponent (d) of 1.96. For intermediate values of L (SEM and XMT; $2 \times 10^{-2} < L < 5 \times 10^{-1}$ mm), d increases to 3.24 and 3.28 respectively. For large values of L (XMT; L > 5×10^{-1} mm), d decreases to 2.06.

The average melt corrected total vesicle number density (N$_{V,tot}$^{melt}) from SEM images is 2.52×10^{6} mm^{-3}, which is two orders of magnitude larger than the value of 4.23×10^{4} mm^{-3} from XMT images (Table 2). N$_{V,tot}$^{melt} values are dominated by the smallest vesicles, which can be artificially combined by XMT when image resolution is insufficient to capture the finest of melt films or artificially separated by SEM when complicated vesicles are counted multiple times on a 2D surface. When N$_{V,tot}$^{melt} is calculated using vesicles of $2 \times 10^{-2} < L < 2 \times 10^{-1}$ mm (the resolution range covered well by both techniques), the XMT and SEM datasets show close agreement.

The spatial correlation between crystals and moderately large vesicles identified qualitatively (Fig. 5c) was tested further in A$_{10}$ and C$_{10}$ as they contain the most crystals and were imaged with a resolution appropriate for capturing larger vesicles. The N$_V$ versus L relationship of all vesicles was compared to that of the 100 vesicles closest to each crystal quantified using 3D nearest neighbour analysis implemented in the SpatStat package in R (Baddeley and Turner, 2005). Due to small instabilities during repeated iterations of nearest neighbour calculations, N$_V$ versus L systematics of near-crystal vesicles are presented as a field rather than a single line (Fig. 9). Vesicles near crystals have larger modal equivalent diameters by ~1.5×10^{-1} mm, verifying previous qualitative assessments.

5. Discussion

5.1. Comparison of results from SEM and XMT

By combining SEM and XMT imaging, we were able to obtain high spatial resolution images (SEM) as well as quantifying 3D relationships between objects (XMT). When applying any method with a finite spatial resolution, a population of small features may always be beyond the limits of imaging resolution. The resolution (and contrast) of the XMT data was insufficient to determine the finest of vesicle walls and the presence, or in this case absence, of microlites. Region of interest scanning, or higher resolution XMT laboratory systems, can yield 3D datasets with voxel resolutions down to 50 nm which would allow SEM-comparable imaging of thin vesicle walls, albeit within much smaller 3D volumes. However, the large, heterogeneously distributed high density crystals (aegirine augite, Fe-Ti oxides and aenigmatite) increased image noise and thus prevented observation of fine scale structures in these samples. In highly porous samples, like those investigated here, XMT image analysis generally underestimates vesicle number densities, primarily by the over-coalescence of neighbouring vesicles. Direct comparison of volcanological interpretations from SEM and XMT multiscale data should therefore be made with caution. For example, multiscale imaging studies of basaltic scoria and bombs from Villarrica observed discrepancies between SEM- and XMT-derived N$_{V,tot}$ values of a similar magnitude to those we observe at Pantelleria (Gurioli et al., 2008). In contrast, in datasets where vesicles are large with respect to the XMT voxel resolution, SEM and XMT datasets may agree well with each other, as reported in pumices from Montserrat (Giachetti et al., 2011). Imaging using any method (optical, SEM, XMT, etc.) where the smallest feature (vesicle or vesicle wall) is less than three pixels/voxels in diameter will be subject to significant uncertainty (Lin et al., 2015).

Segmentation and separation of the vesicles in the 3D dataset were performed by automated methods (20–60 min per step, per sample), and were entirely parameterised from the data. The processing of XMT data therefore avoided the time-consuming manual rectification required for SEM data (>16 h per sample) and eliminates user-induced bias for feature recognition. The good agreement between the VSDs from both methods (Fig. 8c) indicates that our SEM and XMT datasets can be combined to extend the range of L. Using XMT scans at two resolutions, it is theoretically possible to constrain VSDs over at least five orders of magnitude of equivalent diameter (beyond the 10^{3} range observed in our sample). XMT is able to accurately define the volume of all vesicles (within the image resolution) without using stereological

Table 2
Vesicle and crystal data from SEM and XMT.

Sample	Density (g·cm^{-3})	Porosity (vol.%)	Vesicularity (vol.%)	Proportion elongate vesicles	Crystal (vesicle free) (vol.%)	Crystal aspect ratio	Microlite (vol.%)	$N_{A,tot}$ (mm^{-2})	$N_{v,tot}$ MCN93 (mm^{-3})	$N_{v,tot}^{melt}$ MCN93 (mm^{-3})	$N_{v,tot}$ SP98 (mm^{-3})	$N_{v,tot}^{melt}$ SP98 (mm^{-3})	$N_{v,tot}$ XMT (mm^{-3})	$N_{v,tot}^{melt}$ XMT (mm^{-3})
A$_{10}$	0.58	76.9	79.2	0.49	2.62 (11.4)	2.48	0	2.51×10^3	7.26×10^5	3.14×10^6	6.14×10^5	2.66×10^6		
A$_5$	0.58	76.9	77.6	0.50	3.99 (17.3)	2.36	0	2.41×10^3	7.00×10^5	3.03×10^6	6.03×10^5	2.61×10^6		
C$_{10}$	0.60	76.0	83.0	0.33	3.81 (16.1)	2.44	0	1.98×10^3	6.49×10^5	2.70×10^6	5.80×10^5	2.42×10^6		
C$_5$	0.67	73.8	73.5	0.62	2.82 (10.8)	2.02	0	2.29×10^3	7.29×10^5	2.78×10^6	6.16×10^5	2.35×10^6		
Average	0.60	76.2	78.2	0.44	3.24 (13.7)	2.41	0	2.34×10^3	7.05×10^5	2.93×10^6	6.08×10^5	2.52×10^6	1.02×10^4	4.23×10^4

Porosity is calculated using the bulk density measurements with volumes measured from low resolution XMT images. Vesicularity and microlite content are calculated from the highest resolution SEM images.
Elongate vesicle defined as having long axis to short axis ratio >2.
Crystal content and aspect ratios are calculated from XMT images.
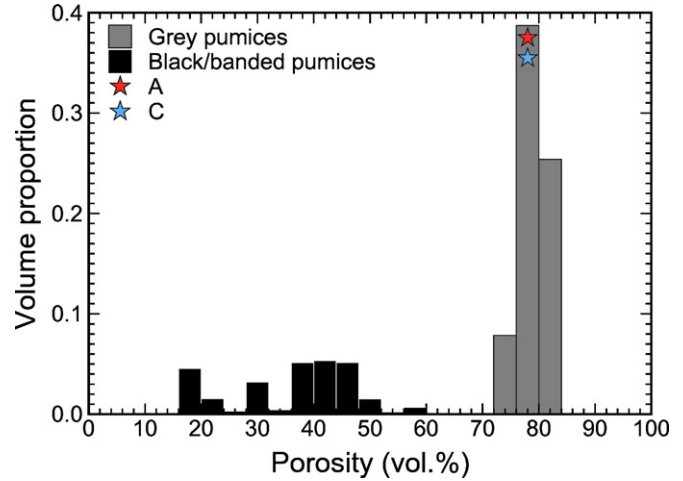
Fig. 3. Porosity distribution of juvenile material from the Cuddia di Mida second airfall deposit (09PNL001) coloured for grey and black/mixed clasts. The porosity of clasts A (red) and C (blue) are highlighted.

corrections. This is particularly important for non-spherical elongate or coalesced vesicles, which are treated poorly by standard stereological conversions applied to 2D data. For ellipsoidal vesicles, vesicle volume calculated assuming sphericity using the 2D cross-section can significantly over or underestimate volume depending on orientation relative to the 2D section plane. Vesicles with highly complex morphologies can be counted multiple times depending on their intersection with the plane of the 2D section, affecting size distributions and number densities (e.g., Sahagian and Proussevitch, 1998). The limited sample area of 2D analyses impacts on the structural information extracted, and 3D imaging is critical for textural studies (Giachetti et al., 2011; Baker et al., 2012). This is highlighted by sample C$_5$, where the strong, localised and variably oriented fabric visible in the XMT images is entirely missed by the SEM data acquired in a single plane through the same sample volume. 3D imaging also allowed us to quantify spatial correlations between vesicles and crystals, which was not possible from 2D data due to the limited number of crystals intersected in single slices.
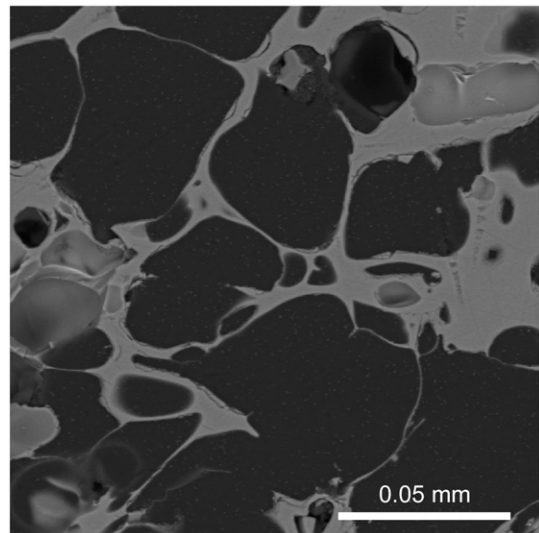
Fig. 4. SEM image at the highest resolution showing the absence of any microlites. Vesicles are black and melt is grey.
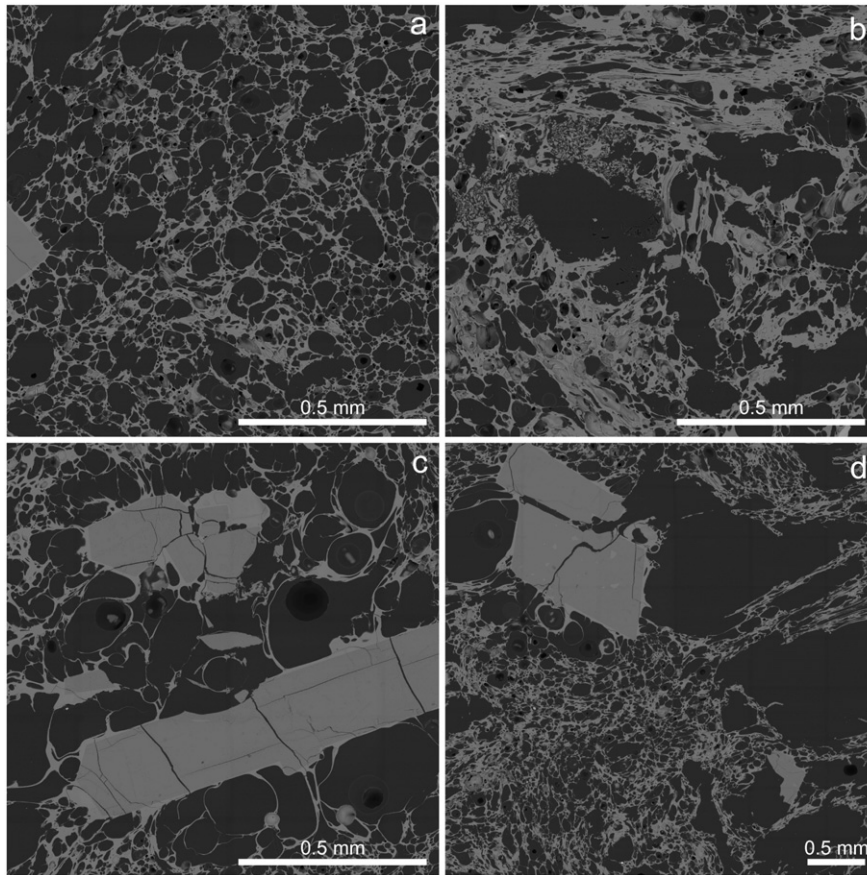
Fig. 5. SEM images highlighting the different vesicle textures found in both the SEM and XMT images: a) polyhedral foam; b) sub-spherical, thicker walled vesicles; c) vesicles attached to crystal faces; and d) large vesicles with convoluted faces. Vesicles are black and melt/crystals are grey.

5.2. Bubble nucleation, growth and deformation recorded in pumice textures

Grey pumices exhibit a narrow range of porosities (78.9 ± 2.4 vol.%) and are texturally similar to one another – they have VSDs that are within error over the full range of L. The modal density of the grey pumices (0.5–0.6 g·cm^{-3}) is similar to the Oira pumice cone (0.5–0.6 g·cm^{-3}) and Ruru Pass Tephra (0.4–0.5 g·cm^{-3}) of Mayor Island, NZ, both magmatic peralkaline eruptions of Strombolian-to-Hawaiian intensity (Houghton et al., 1987). The power-law relationships in the cumulative VSD data imply non-equilibrium, continuous and/or accelerating nucleation and growth of bubbles; conditions common during explosive eruptions of silica-rich magmas (e.g., Mangan and Cashman, 1996; Blower et al., 2001, 2003). Power law exponents (d) of <2 have been shown experimentally to represent continuous nucleation and free growth of bubbles (Blower et al., 2001, 2003); we suggest that the smallest vesicles (L < 2 × 10^{-2} mm; d = 1.96) originated in this way. This value of d is comparable to those reported for vesicles of a similar size from Askja 1875 (Carey et al., 2009) and Chaitén 2008 (Alfano et al., 2012) (Table 4), where bubble development is thought to reflect a final stage of rapid decompression that occurred shortly before fragmentation at a high degree of vapour supersaturation. For intermediate vesicle sizes (2 × 10^{-2} < L < 5 × 10^{-1} mm), our peralkaline samples have a power law exponent of ~3.25, a change in slope which may have been caused by bubble coalescence overprinting continuous nucleation (Gaonac'h et al., 1996), a process that has been reported for Askja 1875 (Carey et al., 2009), Chaitén 2008 (Alfano et al., 2012), Mount Mazama 7700 BP (Klug et al., 2002) and Taupo 1.8 ka (Houghton et al., 2010) (Table 4). This intermediate-sized population

of vesicles includes heterogeneously distributed bubbles that we interpret as having nucleated early on phenocrysts at low degrees of supersaturation (Figs. 5c and 9). Our largest vesicle population (L > 5 × 10^{-1} mm) returns to a power law exponent typical of continuous nucleation and free growth (d = 2.06), which we suggest could be related to dynamic processes such as tearing and deformation during fragmentation, but has not been noted in previous studies.

There is a high degree of spatial heterogeneity in vesicle deformation over small length scales (<1 mm), suggesting that strain was localised (Wright and Weinberg, 2009). This is especially noticeable in C$_5$ (Fig. 7). The presence of deformed, elongated vesicles (with elongation factors often > 10) suggests that maximum strain rates during the eruption were locally much higher than those that would be calculated using bulk parameters (e.g., conduit radius and volume flux). However, the larger, near-crystal vesicle population shows little or no deformation, which suggests the possible formation of strain shadows around crystals. The spatial relations between crystals and deformation require further investigation before this can be quantified.

To compare vesicle textures of the Cuddia di Mida eruption with those from other eruptions, literature data from a variety of magmatic (i.e., not phreatomagmatic) eruptions are shown in Fig. 10. Fig. 10a displays N$_V$ versus melt SiO$_2$ content for a wide range of magma compositions (basalt to rhyolite) and eruption styles (Strombolian to Plinian). In general, rhyolitic eruptions have higher N$_V$ than basaltic eruptions, although some basaltic Plinian eruptions reach values similar to rhyolitic eruptions. Within basaltic eruptions, Plinian eruptions tend to have higher N$_V$ than Strombolian events but the values do overlap. Conversely, N$_V$ for rhyolitic eruptions does not correlate with eruption style as the small cone-forming events have N$_V$ values similar to those from
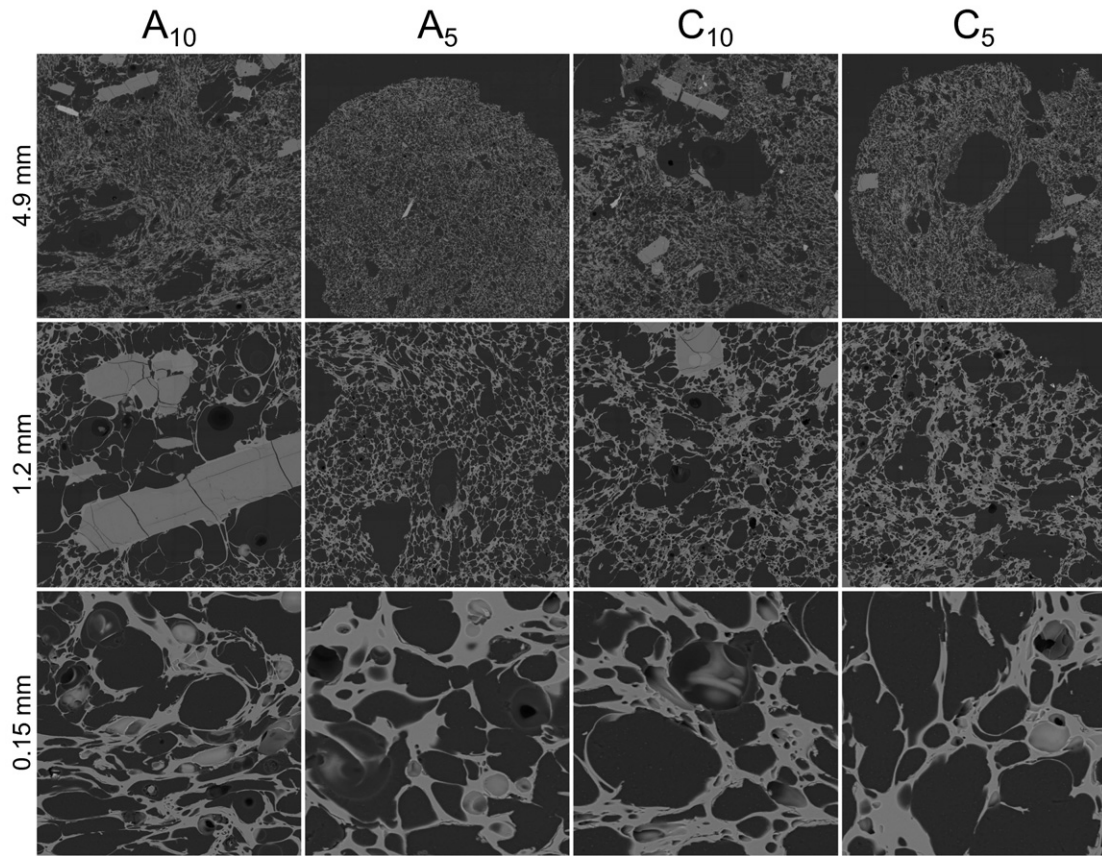
Fig. 6. Selected SEM images with increasing resolution from top to bottom (field of view shown along the left hand side). Vesicles are black and melt/crystals are grey. Sample letter shown along the top. All slices are in the XY plane of the XMT data (Fig. 7). Images shown are not necessarily stacked in order to represent typical textures at equivalent resolutions.

sub-Plinian and Plinian events. For example, the Cuddia di Mida eruption has N_V values similar to those from a small cone-forming rhyolitic eruption on Raoul (Rotella et al., 2014) and from sub-Plinian to Plinian rhyolitic eruptions. These values are one-to-four orders of magnitude larger than basaltic Strombolian eruptions and at the maximum values for basaltic Plinian eruptions. However, the total vesicle number densities we report for the Cuddia di Mida eruption are an order of magnitude larger than those reported from member A of the peralkaline Green Tuff eruption by Campagnola et al. (2016).

Fig. 10b and c only include a sub-set of the eruptions used in Fig. 10a selected to represent data from two end-member fragmentation mechanisms (Gonnermann, 2015): inertia-driven break-up of low viscosity melt (e.g., basaltic Strombolian) and strain-induced brittle failure (e.g., crystal-free rhyolitic Plinian). Crystal-free rhyolitic eruptions were chosen as the Cuddia di Mida eruption contains only a minor phenocryst component and no microlites, implying that a high crystal content did not lead to fragmentation. As expected, comparing N_V to melt viscosity (Fig. 10b) shows a very similar trend to comparing to melt SiO_2 content.

Small peralkaline eruptions have been compared to basaltic Strombolian eruptions in previous work due to their low viscosities (e.g., Houghton et al., 1985a). However, the viscosity and N_V of the Cuddia di Mida eruption are much more similar to rhyolitic eruptions than basaltic Strombolian eruptions. This may be due to the lower diffusivities of volatile species through cooler rhyolitic melts influencing bubble nucleation and growth: with slower diffusion it is easier to nucleate new bubbles than to diffuse volatiles into existing bubbles, which results in higher N_V (Sparks, 1978).

Fig. 10c shows vesicle size distributions (VSDs) for rhyolitic sub-Plinian to Plinian and basaltic Strombolian eruptions as well as our data from the Cuddia di Mida eruption. VSDs from single eruptions are similar to each other, but VSDs do not appear to correlate with eruption style or magma composition in general. Basaltic Strombolian eruptions tend to have larger vesicles compared to rhyolitic eruptions but rhyolitic eruptions also span wide ranges of vesicle sizes. However, our samples from Cuddia di Mida are more similar to those from rhyolitic eruptions than from basaltic Strombolian eruptions because they contain many small vesicles that are absent in the basaltic eruptions.

The low viscosity of the peralkaline Cuddia di Mida melt does not appear to have exerted a major control on the final vesicle textures of the pumices (Figs. 5 and 10). That is, the peralkaline rhyolites studied here resemble deposits from silica-rich, calc-alkaline eruptions with much higher melt viscosities, particularly with respect to minimum vesicles sizes and strain localisation features (see studies on Chaitén 2008 and the Campanian Ignimbrite from Alfano et al. (2012) and Polacci et al. (2003) respectively). The pumice textures do not resemble those of scoria from basaltic, Strombolian eruptions at Stromboli or Villarrica, which are characterised by much larger vesicles (Gurioli et al., 2008; Lautze and Houghton, 2005, 2006, 2008; Polacci et al., 2009; Leduc et al., 2015). Furthermore, the $N_{V,tot}^{melt}$ values and VSDs calculated are similar to those from the products of high-silica calc-alkaline eruptions of varying size (Table 4, Fig. 10).

5.3. The fragmentation mechanism of peralkaline magmas

Interaction with external water is not considered to be a viable fragmentation mechanism for the Cuddia di Mida eruption due to the lack of field evidence for magma-water interaction (Mahood and Hildreth, 1986). Furthermore, pumice clasts from Cuddia di Mida lack the fluidal shapes associated with inertia-driven fragmentation of the type observed in Hawaiian eruptions (Namiki and Manga, 2008); and the total vesicle number density is one–to–four orders of magnitude larger than those found in the products of basaltic Strombolian eruptions.
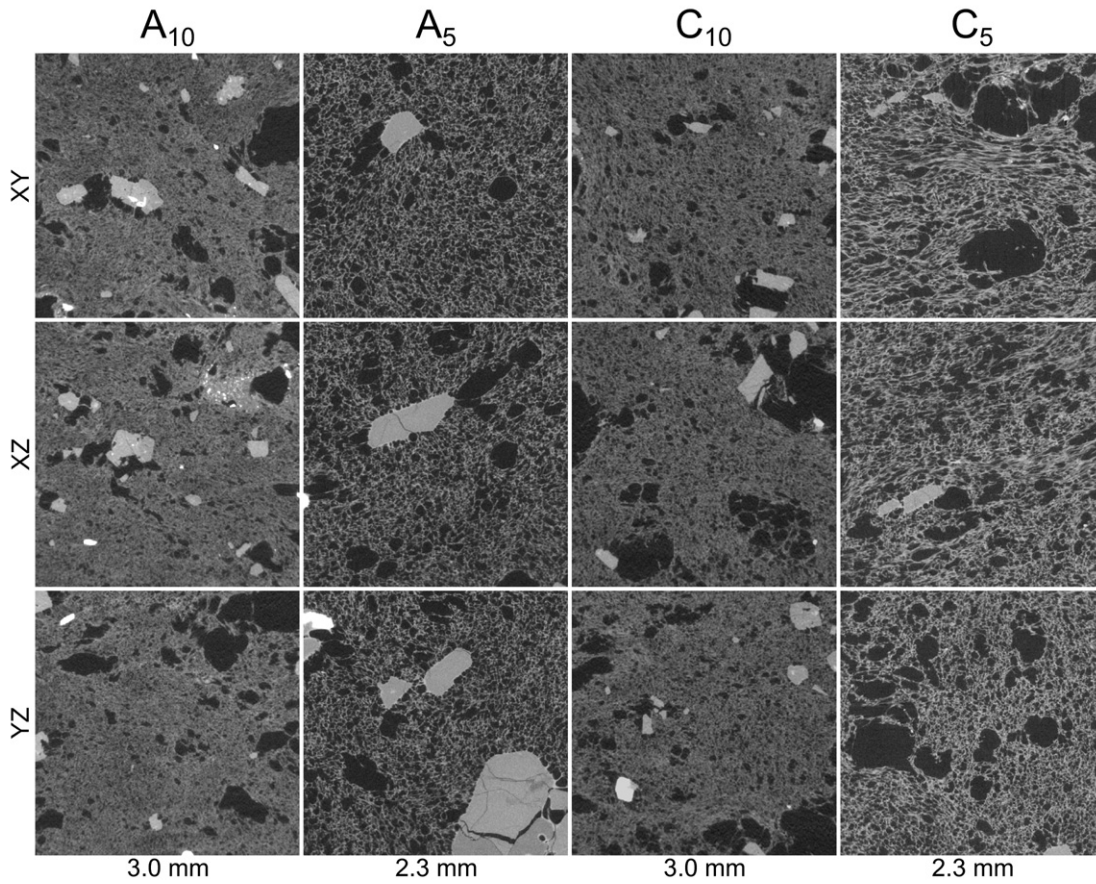
Fig. 7. Selected orthogonal 2D slices through the 3D XMT images with field of view shown along the bottom. Vesicles are black, melt/feldspars/pyroxenes are grey and oxides are white. Sample letter shown along the top. Arbitrary slice orientation shown on the left hand side.
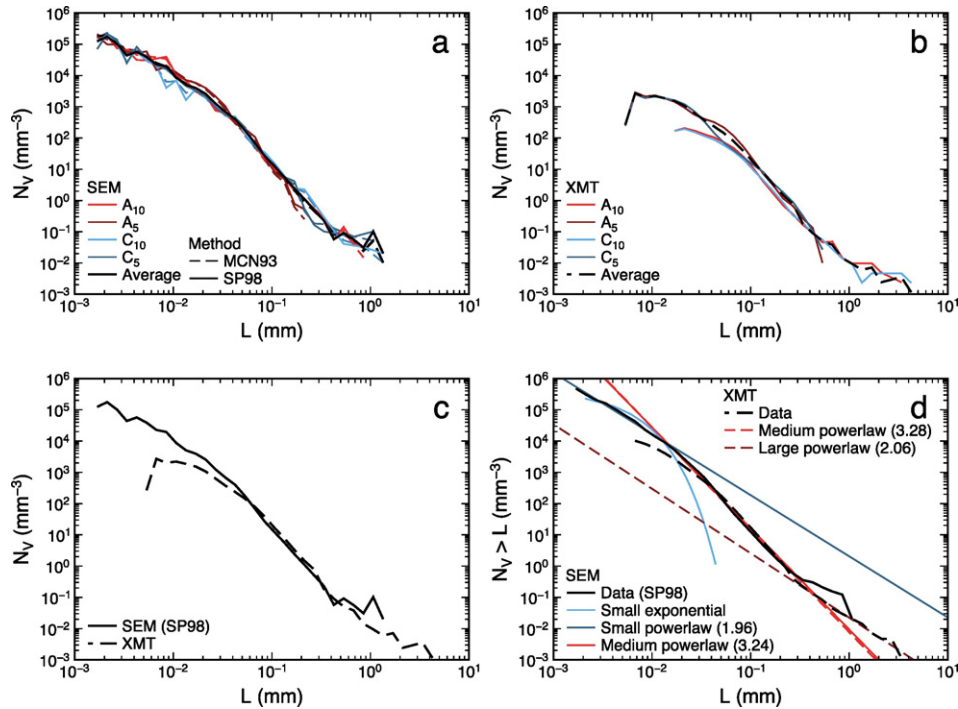
Fig. 8. Vesicle size distributions (VSDs) with respect to equivalent diameter (L) for SEM and XMT data: a) SEM generated VSDs (N_V) stereologically corrected using Mangan et al. (1993) (MCN93, dashed line) and Sahagian and Proussevitch (1998) (SP98, solid line); b) XMT generated VSDs (N_V); c) comparison of VSDs generated by SEM and XMT; and d) comparison of cumulative VSDs ($N_V > L$) for SEM and XMT showing exponential and power law fits, where small, medium and large in the legend refers to the vesicle sizes.

Table 3
Power law exponents (d) and vesicle equivalent diameter (L) break in slope values for small (s), medium (m) and large (l) vesicle populations using SEM and XMT data.

	L_{s-m} (mm)	L_{m-l} (mm)	d_s	d_m	d_l
SEM	2.5×10^{-2}			1.96	3.24
XMT		5.0×10^1		3.28	2.06

Therefore tearing apart of melt by bubble bursting is also not a viable fragmentation mechanism (Fig. 10; Gonnermann, 2015). Textural similarities between peralkaline and calc-alkaline pumices thus suggest similar brittle fragmentation mechanisms, despite differences in chemistry and physical properties.

Magmas fragment in a brittle fashion when a critical, viscosity-dependent strain-rate is exceeded (Papale, 1999). Bulk magma viscosity depends on melt composition and on magma crystallinity and vesicularity (e.g., Rust and Manga, 2002; Giordano et al., 2008; Vona et al., 2011; Mader et al., 2013). Magma water content decreases dramatically during decompression and degassing, increasing the bulk viscosity (Giordano et al., 2008) and bringing the magma closer to fragmentation. Assuming that the melt was largely degassed at the point of fragmentation, we use the PS-GM viscosity model of Di Genova et al. (2013) to calculate a melt viscosity range of $10^{4.28}$ to $10^{7.11}$ Pa·s (at 0.0–1.0 wt.% water) at a temperature of 1075 K (Neave et al., 2012). The PS-GM viscosity model is based on a modified Vogel-Fulcher-Tammann equation and is specifically calibrated for peralkaline compositions (Di Genova et al., 2013). Including crystals (13.8 vol.%, average aspect ratio of 2.4) has a negligible effect on the bulk viscosity ($10^{4.65}$ to $10^{7.48}$ Pa·s at 0.0–1.0 wt.% water; Mader et al., 2013).

Samples contain elongate vesicles (33–62% of total vesicle populations) which implies that melt capillary numbers were high and that the bulk viscosity decreased with increasing bubble content (Rust and Manga, 2002). At the high vesicle volume fractions observed here (~76 vol.%), the standard models that relate viscosity to porosity are not applicable (they remain robust up to a maximum porosity of 50 vol.%; Mader et al., 2013). It is therefore not possible to calculate the bulk viscosity at the moment of fragmentation precisely. However, assuming that the melt had an initial water content of 5 wt.% (Neave et al., 2012), contained 13.7 vol.% crystals when resident in the magma chamber at 1.5 kbar (Neave et al., 2012) and carried only a negligible volume of pre-existing bubbles, we calculate a bulk viscosity of $10^{1.54}$ Pa·s prior to decompression (1075 K, Neave et al., 2012). If there was no melt-bubble separation during the initial ascent, the viscosity, bubble content and pressure-dependent melt water content up to the 50 vol.% porosity threshold can be estimated (the porosity threshold is estimated to occur at ~25 bars; Papale et al., 2006). Beyond this
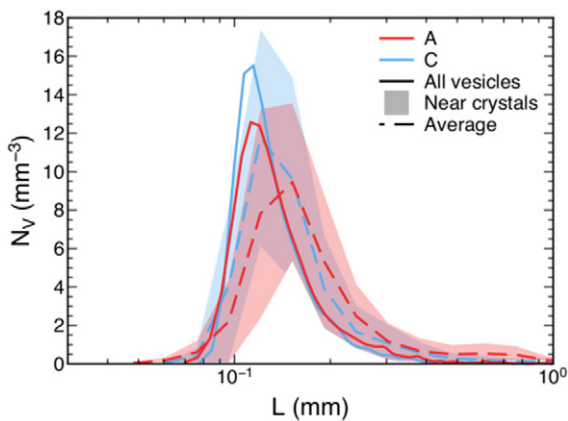
Fig. 9. Vesicle size distribution (VSDs) for all vesicles (solid line) and vesicles next to crystals (average indicated by the dashed line and range indicated by the filled region) for A (red) and C (blue).

threshold we cannot assess the effect of bubbles on viscosity and therefore a maximum estimate for the viscosity of the bulk magma containing 50 vol.% bubbles at fragmentation is $10^{4.15}$ to $10^{6.61}$ Pa·s (assuming 0.0–1.0 wt. % water at 1075 K; Mader et al., 2013).

The minimum bulk viscosity (μ) required for strain-induced fragmentation is defined as $\mu \geq (CG_\infty \pi r^3 / Q)^{(1/0.9)}$, where r is the conduit radius (m), Q is the volume flux (m^3·s^{-1}), G_∞ is the elastic modulus at infinite frequency (10 GPa) and C is a fitting parameter (0.01 (Pa·s)$^{-0.1}$) (Gonnermann and Manga, 2003). For a realistic conduit radius of 10 m (e.g., Campagnola et al., 2016) a mass flux of 2.4×10^8 to 3.5×10^{10} kg·s^{-1} (equivalent to a volume flux of 3.5×10^5 to 5.8×10^7 m^3·s^{-1}) is required to achieve the minimum strain rate required for fragmentation when considering the viscosities calculated above ($10^{4.15}$ to $10^{6.61}$ Pa·s). These should be considered as minimum mass flux estimates as bulk viscosity will likely be reduced further at higher vesicle contents (~25 vol.% of measured porosity beyond the model limits, Mader et al., 2013). The much larger Green Tuff eruption had a comparable viscosity to the Cuddia di Mida eruption during the earliest explosive, crystal-poor part of the eruption (Campagnola et al., 2016), yet the mass fluxes we calculate to be necessary for fragmentation are much larger than those estimated for both the entire Green Tuff eruption (~2×10^8 kg·s^{-1}; Williams et al., 2013), and member A of the Green Tuff (9.3×10^5 kg·s^{-1}; Campagnola et al., 2016) and are therefore unfeasible. Conversely, achieving fragmentation using the lower bound of the published mass fluxes for these eruptions would require a conduit radius of <1 m. Assuming strain-induced fragmentation, the calculated minimum mass fluxes and conduit radii required for fragmentation in both small (Cuddia di Mida) and large (Green Tuff) eruptions of peralkaline rhyolite respectively are thus geologically unrealistic.

An alternative mechanism invokes bubble overpressure causing strain-induced fragmentation when gas is unable to expand over the timescale of decompression due to the tensile strength of the surrounding melt (Zhang, 1999; Spieler et al., 2004; Mueller et al., 2008). Although there is no permeability data available for the Cuddia di Mida pumice, the overpressure required for fragmentation (ΔP_{fr}; MPa) can be calculated from $\Delta P_{fr} = \sigma_m / \varphi$ using the known porosity (φ) and magma tensile strength ($\sigma_m = 0.995$ MPa; Spieler et al., 2004). With a porosity of 76 vol.%, the Cuddia di Mida pumices require a bubble overpressure of 1.3 MPa to cause fragmentation. Bubble overpressure is a function of decompression rate and melt viscosity (Barclay et al., 1995). An $N_{V,tot}^{melt}$ of 2.5×10^6 mm^{-3} implies decompression rates of the order 10^7 Pa·s^{-1} (Toramaru, 2006), and the melt viscosity gives relaxation times (τ_s) of 1.9×10^{-6} to 1.3×10^{-3} s for 1.0–0.0 wt.% water using the expression $\tau_s = \mu_s / G_\infty$ (Dingwell and Webb, 1989). The onset of non-Newtonian, unrelaxed, viscoelastic behaviour at 1.9×10^{-4} to 1.3×10^{-1} s, thus implies that average decompression rates of 1.0×10^7 to 6.9×10^9 Pa·s^{-1} are required for fragmentation. Even the lower of these estimates (for the most viscous melt) is extreme, and significantly larger than the value estimated for member A of the Green Tuff eruption (3.82×10^6 Pa·s^{-1}; Campagnola et al., 2016).

Rapid decompression following edifice collapse has been suggested to explain the explosive behaviour of other magmas with seemingly insufficient viscosity to fragment (e.g., ~10^6 to 10^8 Pa·s for Chaitén 2008; Castro and Dingwell, 2009; Alfano et al., 2012). However, edifice collapse is not a viable mechanism for driving rapid decompression on Pantelleria, where cone-forming events have defined recent silicic volcanism. Instead, the high volatile content and low viscosity of peralkaline magmas may play a crucial role in promoting rapid decompression during the initial stages of eruption.

Our 3D XMT data show significant, localised bubble deformation, implying that substantial partitioning of strain across heterogeneous samples took place prior to fragmentation. Strain localisation entails a complex interaction of shear heating (decreasing viscosity) and volatile solubility modification (increasing viscosity) that can drive gas exsolution (increasing or decreasing viscosity depending on strain rate),

Table 4

Summary table for crystal-poor rhyolitic, basaltic Strombolian and peralkaline eruptions.

References: Cuddia di Mida, Pantelleria: Neave et al. (2012), this study; Stromboli, Italy: Metrich et al. (2001), Lautze and Houghton (2005, 2007), Polacci et al. (2009), Leduc et al. (2015); Villarica, Chile: Gurioli et al. (2008); Vesuvius, Italy: Cioni et al. (2011); Raoul, KA: Barker et al. (2012), Rotella et al. (2014); Askja, USA: Sigurdsson and Sparks (1981), Carey et al. (2009); Chaitén, Chile: Castro and Dingwell (2009), Alfano et al. (2012); Mount Mazama, USA: Bacon and Druitt (1988), Klug et al. (2002); Mount St. Helens, USA: Rutherford et al. (1985), Klug and Cashman (1994); Pantelleria, Italy: Campagnola et al. (2016); Taupo, NZ: Sutton et al. (1995), Houghton et al. (2010). A more complete dataset is available in Supplementary material 2.

Volcano	Melt SiO$_2$ (wt.%)	AI	Log [Anhydrous melt viscosity, (Pa·s)]	Vesicle content (vol.%)	Crystal content (vol.%)	Microlite content (vol.%)	N$_{v,tot}^{melt}$ ($\times 10^6$ mm^{-3})	d$_1$	d$_2$
Small cone-forming									
Cuddia di Mida, Pantelleria	70.7	2.23	6.80	78.5	3.2	0	2.5	2.0	3.3
Raoul, KA	69.3	0.51	8.12	82.3	<5	<1	3.0	n.d.	3.9
Strombolian									
Stromboli, Italy	52.2–52.5	0.59–0.64	3.10–3.54	24–78	12–35	<1	0.000096–0.030	n.d.	0.7–1.3
Villarica, Chile	53.9–54.4	0.43–0.45	2.80–2.85	47.9–88.8	1.12–19.8	<1	0.00074–0.014	n.d.	n.d.
Violent Strombolian									
Vesuvius, Italy	46.7	0.67	2.66	43.2–46.3	28.7–39.1	Low	0.018–0.12	n.d.	n.d.
Sub-Plinian to Plinian									
Askja, USA	71.0–72.4	0.72–0.80	6.50–6.68	77.6–88.5	<0.5	0	0.71–2.4	1.6–2.1	3.0–5.1
Chaitén, Chile	74.2	0.73	10.61	43–80	<1	Rare	0.064–0.23	1.0–1.7	3.5–4.2
Mount Mazama, USA	70.4	0.76	8.28	78.5–85.0	10	0	0.36–6.0	n.d.	3.3
Mount St. Helens, USA	72.7–79.6	0.67–0.93	8.15–9.35	55.6–80.7	6–15	0–7	0.82–2.0	n.d.	n.d.
Pantelleria, Italy	62.7–69.4	1.0–1.8	6.52–7.28	78–81	8–22	0–11	0.026–0.35	n.d.	n.d.
Raoul, KA	68.0–69.0	0.44–0.48	7.53–8.06	34.7–88.6	<5	<22	0.98–19	n.d.	3.6–4.0
Taupo, NZ	73.7	0.76	9.85	44–89	2–3.5	Sparse	0.019–4.8	n.d.	3.2

AI is agpaitic index (Na$_2$O + K$_2$O) / Al$_2$O$_3$ in mol.%; viscosity is for the melt phase, excluding the effects of bubbles, crystals and microlites using Giordano et al. (2008) and Di Genova et al. (2013); vesicle, crystal and microlite content are relative to total volume; N$_{v,tot}^{melt}$ is the total vesicle number density corrected for vesicularity; and power law exponents (d) are for the smaller (1) and larger (2) vesicle populations.

elastic stress unloading and changes in the rheological behaviour of vesicles (Wright and Weinberg, 2009). These shear bands have been observed in low viscosity magmas, such as phonolites from Vesuvius, and are thought to develop in the conduit due to lateral velocity gradients and cause outgassing (Shea et al., 2012, 2014). These processes result in a variable and highly heterogeneous rheology on a range of
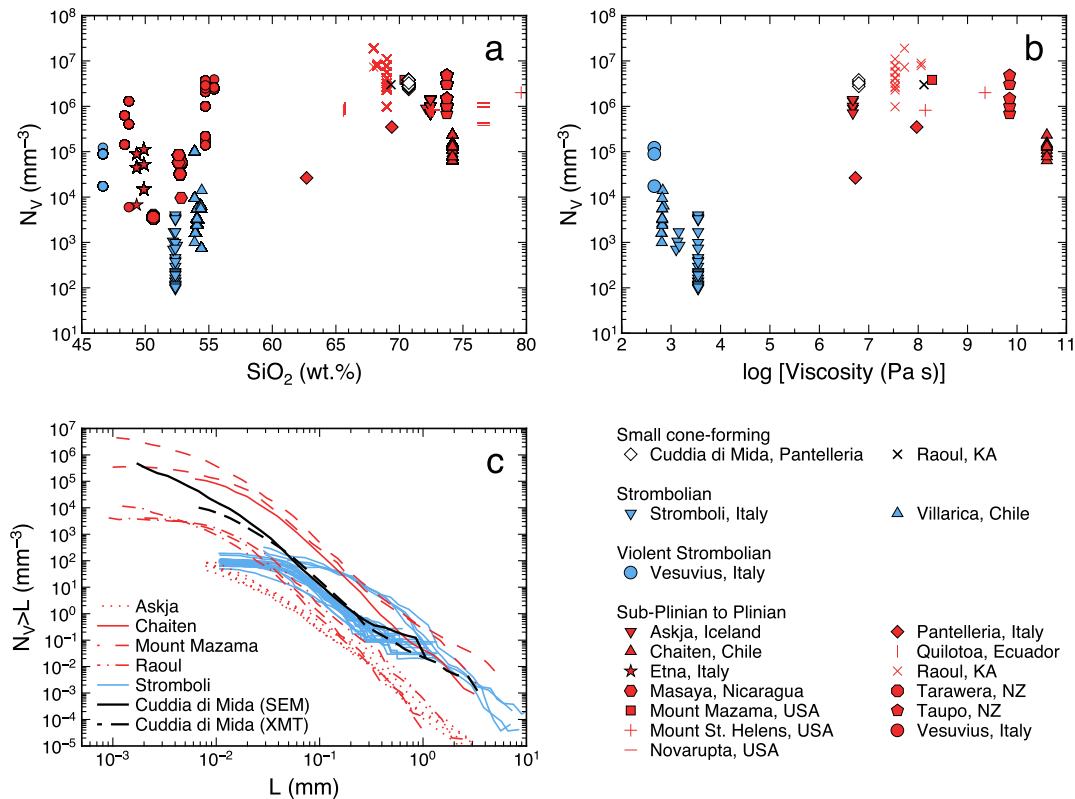
Fig. 10. a) Effect of melt composition (silica content) on total melt corrected vesicle number density (N$_{v,tot}^{melt}$) for various eruption styles; comparison of crystal-poor rhyolitic, basaltic Strombolian and peralkaline eruptions for b) N$_{v,tot}^{melt}$ variation with anhydrous melt viscosity; c) comparison of cumulative melt corrected VSD (N$_v^{melt}$ > L). Viscosities calculated using Giordano et al. (2008), except in the case of Pantelleria where Di Genova et al. (2013) was used.

References: Sigurdsson and Sparks (1981), Rutherford et al. (1985), Klug and Cashman (1994), Sutton et al. (1995), Metrich et al. (2001), Klug et al. (2002), Landi et al. (2004), Lautze and Houghton (2005, 2007), Adams et al. (2006), Sable et al. (2006, 2009), Gurioli et al. (2008), Carey et al. (2009), Castro and Dingwell (2009), Polacci et al. (2009), Costantini et al. (2010), Houghton et al. (2010), Cioni et al. (2011), Rotella et al. (2014), Alfano et al. (2012), Barker et al. (2012), Neave et al. (2012), Leduc et al. (2015), Campagnola et al. (2016) and this study.

spatial and temporal scales, and a consequently variable fragmentation criterion at the bubble-wall scale. Therefore, strain localisation could have permitted fragmentation to have occurred at a lower *bulk* viscosity than calculated above, but requires further empirical and theoretical investigation.

6. Conclusions

By investigating the textures of pumices erupted from the Cuddia di Mida vent on Pantelleria, Italy, we have inferred that, despite having bulk magma viscosities seemingly far too low, peralkaline magmas fragment by brittle failure. Integrating multiscale 2D and 3D analysis techniques on pumice samples allowed vesicle size and shape distribution characteristics to be defined across a wide range of equivalent vesicle diameters. The textures, bulk porosity, VSDs and $N_{V,tot}^{melt}$ values of pumices from Cuddia di Mida are comparable with those from calc-alkaline rhyolite deposits, and imply that, despite the difference in viscosity between calc-alkaline and peralkaline rhyolites, both magma types fragment by strain-induced brittle fragmentation. We show that initial nucleation occurred on large crystals at low degrees of volatile supersaturation. This was followed by some degree of coalescence and textural maturation before homogeneous, continuous nucleation occurred during rapid ascent at higher degrees of volatile supersaturation. Our data also show a possible third regime for the largest vesicles. We show that microlite-free peralkaline pumices cannot reach classically defined fragmentation conditions under even the most extreme of permitted geological conditions, and mechanisms such as bubble overpressure driven by rapid decompression and strain localisation around crystals are suggested instead. The very high decompression rates suggested by our analysis may be aided by the high volatile content and low viscosity of peralkaline magmas.

Author contributions

The project was conceived by ME, following the work of DAN. The manuscript arose from the M.Sci. (Cambridge) thesis of ECH. DAN collected the samples and processed the SEM dataset. ECH acquired the XMT data and performed the analysis under the supervision of KJD. PJW provided access to the MXIF. ECH led manuscript production with further contribution from all authors.

Acknowledgements

Appendix A. Supplementary data

Supplementary data to this article can be found online at http://dx.doi.org/10.1016/j.jvolgeores.2017.02.020.

References

Adams, N., Houghton, B., Hildreth, W., 2006. Abrupt transitions during sustained explosive eruptions: examples from the 1912 eruption of Novarupta, Alaska. Bull. Volcanol. 69 (2):189–206. http://dx.doi.org/10.1007/s00445-006-0067-4.

Alfano, F., Bonadonna, C., Gurioli, L., 2012. Insights into eruption dynamics from textural analysis: the case of the May, 2008, Chaitén eruption. Bull. Volcanol. 74 (9): 2095–2108. http://dx.doi.org/10.1007/s00445-012-0648-3.

Bacon, C.R., Druitt, T.H., 1988. Compositional evolution of the zoned calcalkaline magma chamber of Mount Mazama, Crater Lake, Oregon. Contrib. Mineral. Petrol. 98 (2): 224–256. http://dx.doi.org/10.1007/BF00402114.

Baddeley, A., Turner, R., 2005. spatstat: an R package for analyzing spatial point patterns. J. Stat. Softw. 12 (6).

Baker, D.R., Mancini, L., Polacci, M., Higgins, M.D., Gualda, G.A.R., Hill, R.J., Rivers, M.L., 2012. An introduction to the application of X-ray microtomography to the three-dimensional study of igneous rocks. Lithos 148:262–276. http://dx.doi.org/10.1016/j.lithos.2012.06.008.

Barclay, J., Riley, D.S., Sparks, R.S.J., 1995. Analytical models for bubble growth during decompression of high viscosity magmas. Bull. Volcanol. 57 (6):422–431. http://dx.doi.org/10.1007/BF00300986.

Barker, S.J., Wilson, C.J.N., Baker, J.A., Millet, M.-A., Rotella, M.D., Wright, I.C., Wysoczanski, R.J., 2012. Geochemistry and petrogenesis of silicic magmas in the intra-oceanic Kermadec Arc. J. Petrol. 54 (2):351–391. http://dx.doi.org/10.1093/petrology/egs071.

Bernard, B., Kueppers, K., Ortiz, H., 2015. Revisiting the statistical analysis of pyroclast density and porosity. Solid Earth 6, 869–879.

Blower, J.D., Keating, J.P., Mader, H.M., Phillips, J.C., 2001. Inferring volcanic degassing processes from vesicle size distributions. Geophys. Res. Lett. 28:347–350. http://dx.doi.org/10.1029/2000GL012188.

Blower, J.D., Keating, J.P., Mader, H.M., Phillips, J.C., 2003. The evolution of bubble size distributions in volcanic eruptions. J. Volcanol. Geotherm. Res. 120 (1–2):1–23. http://dx.doi.org/10.1016/S0377-0273(02)00404-3.

Bottinga, Y., Weill, D.F., 1970. Densities of liquid silicate systems calculated from partial molar volumes of oxide components. Am. J. Sci. 269 (2), 169–182.

Campagnola, S., Romano, C., Mastin, L.G., Vona, A., 2016. Confort 15 model of conduit dynamics: applications to Pantelleria Green Tuff and Etna 122 BC eruptions. Contrib. Mineral. Petrol. 171:60. http://dx.doi.org/10.1007/s00410-016-1265-5.

Carey, R.J., Houghton, B.F., Thordarson, T., 2009. Abrupt shifts between wet and dry phases of the 1875 eruption of Askja Volcano: microscopic evidence for macroscopic dynamics. J. Volcanol. Geotherm. Res. 184 (3–4):256–270. http://dx.doi.org/10.1016/j.jvolgeores.2009.04.003.

Castro, J.M., Dingwell, D.B., 2009. Rapid ascent of rhyolitic magma at Chaitén volcano, Chile. Nature 461:780–783. http://dx.doi.org/10.1038/nature08458.

Catalano, S., De Guidi, G., Lanzafame, G., Monaco, C., Tortorici, L., 2009. Late quaternary deformation on the island on Pantelleria: new constraints for the recent tectonic evolution of the Sicily Channel Rift (southern Italy). J. Geodyn. 48 (2):75–82. http://dx.doi.org/10.1016/j.jog.2009.06.005.

Cioni, R., Bertagnini, A., Andronico, D., Cole, P.D., Mundula, F., 2011. The 512 AD eruption of Vesuvius: complex dynamics of a small scale subplinian event. Bull. Volcanol. 73 (7):789–810. http://dx.doi.org/10.1007/s00445-011-0454-3.

Civetta, L., Cornette, Y., Gillot, P.Y., Orsi, G., 1988. The eruptive history of Pantelleria (Sicily channel) in the last 50 ka. Bull. Volcanol. 50 (1):47–57. http://dx.doi.org/10.1007/BF01047508.

Civetta, L., D'Antonio, M., Orsi, G., Tilton, G.R., 1998. The geochemistry of volcanic rocks from Pantelleria Island, Sicily Channel: petrogenesis and characteristics of the mantle source region. J. Petrol. 39 (8):1453–1491. http://dx.doi.org/10.1093/petroj/39.8.1453.

Civile, D., Lodolo, E., Tortorici, L., Lanzafame, G., Brancolini, G., 2008. Relationships between magmatism and tectonics in a continental rift: the Pantelleria Island region (Sicily Channel, Italy). Mar. Geol. 251 (1–2):32–46. http://dx.doi.org/10.1016/j.margeo.2008.01.009.

Civile, D., Lodolo, E., Accettella, D., Geletti, R., Ben-Avraham, Z., Deponte, M., Facchin, L., Ramella, R., Romeo, R., 2010. The Pantelleria graben (Sicily Channel, Central Mediterranean): an example of intraplate "passive" rift. Tectonophysics 490 (3–4):173–183. http://dx.doi.org/10.1016/j.tecto.2010.05.008.

Costantini, L., Houghton, B.F., Bonadonna, C., 2010. Constraints on eruptions dynamics of basaltic explosive activity derived from chemical and microtextural study: the examples of the Fontana Lapilli Plinian eruption, Nicaragua. J. Volcanol. Geotherm. Res. 189 (3–4), 207–224.

Di Genova, D., Romano, C., Hess, K.-U., Vona, A., Poe, B.T., Giordano, D., Dingwell, D.B., Behrens, H., 2013. The rheology of peralkaline rhyolites from Pantelleria Island. J. Volcanol. Geotherm. Res. 249:201–216. http://dx.doi.org/10.1016/j.jvolgeores.2012.10.017.

Dingwell, D.B., Webb, S., 1989. Structural relaxation in silicate melts and non-Newtonian melt rheology in geologic processes. Phys. Chem. Miner. 16 (5):508–516. http://dx.doi.org/10.1007/BF00197020.

Dingwell, D.B., Hess, K.-U., Romano, C., 1998. Extremely fluid behavior of hydrous peralkaline rhyolites. Earth Planet. Sci. Lett. 158 (1–2):31–38. http://dx.doi.org/10.1016/S0012-821X(98)00046-6.

Gaonac'h, H., Lovejoy, S., Stix, J., Scherzer, D., 1996. A scaling growth model for bubbles in basaltic lava flows. Earth Planet. Sci. Lett. 139 (3–4):395–409. http://dx.doi.org/10.1016/0012-821X(96)00039-8.

Giachetti, T., Burgisser, A., Arbaret, L., Druitt, T.H., Kelfoun, K., 2011. Quantitative textural analysis of Vulcanian pyroclasts (Montserrat) using multi-scale X-ray computed microtomography: comparison with results from 2D image analysis. Bull. Volcanol. 73:1295–1309. http://dx.doi.org/10.1007/s00445-011-0472-1.

Giordano, D., Russell, J.K., Dingwell, D.B., 2008. Viscosity of magmatic liquids: a model. Earth Planet. Sci. Lett. 271 (1–4):123–134. http://dx.doi.org/10.1016/j.epsl.2008.03.038.

Gonnermann, H.M., 2015. Magma fragmentation. Annu. Rev. Earth Planet. Sci. 43: 431–458. http://dx.doi.org/10.1146/annurev-earth-060614-105206.

Gonnermann, H.M., Manga, M., 2003. Explosive volcanism may not be an inevitable consequence of magma fragmentation. Nature 426:432–435. http://dx.doi.org/10.1038/nature02138.

Gurioli, L., Harris, A.J.L., Houghton, B.F., Polacci, M., Ripepe, M., 2008. Textural and geophysical characterization of explosive basaltic activity at Villarrica volcano. J. Geophys. Res. 113:B08206. http://dx.doi.org/10.1029/2007JB005328.

Gurioli, L., Andronico, D., Bachelery, P., Balcone-Boissard, H., Battaglia, J., Boudon, G., Burgisser, A., Burton, M.R., Cashman, K., Cichy, S., Cioni, R., Di Muro, A., Dominguez, L., D'Oriano, C., Druitt, T., Harris, A.J.L., Hort, M., Kelfoun, K., Komorowski, J.C., Kueppers, U., Le Pennec, J.L., Menand, T., Paris, R., Pioli, L., Pistolesi, M., Polacci, M., Pompilio, M., Ripepe, M., Roche, O., Rose-Koga, E., Rust, A., Schiavi, F., Scharff, L., Sulpizio, R., Taddeucci, J., Thordarson, T., 2015. MeMoVolc consensual document: a review of cross-disciplinary approaches to characterizing small explosive magmatic eruptions. Bull. Volcanol. 77:49. http://dx.doi.org/10.1007/s00445-015-0935-x.

Houghton, B.F., Wilson, C.J.N., 1989. A vesicularity index for pyroclastic deposits. Bull. Volcanol. 51 (6):451–462. http://dx.doi.org/10.1007/BF01078811.

Houghton, B.F., Wilson, C.J.N., Weaver, S.D., 1985a. Strombolian deposits at Mayor Island: basaltic eruption styles displayed by a peralkaline rhyolitic volcano. NZ Geol. Surv. Rec. 8, 42–51.

Houghton, B.F., Wilson, C.J.N., Weaver, S.D., 1985b. The Ruru Pass Mayor Tephra, a peralkaline welded air fall tuff from Major Island. NZ Geol. Surv. Rec. 8, 30–36.

Houghton, B.F., Wilson, C.J.N., Weaver, S.D., 1987. The Opo Bay tuff cone, Mayor Island: interaction between rising gas-poor pantelleritic magma and external water. NZ Geol. Surv. Rec. 18.

Houghton, B.F., Weaver, S.D., Wilson, C.J.N., Lanphere, M.A., 1992. Evolution of a quaternary peralkaline volcano: Mayor Island, New Zealand. J. Volcanol. Geotherm. Res. 51: 217–236. http://dx.doi.org/10.1016/0377-0273(92)90124-V.

Houghton, B.F., Carey, R.J., Cashman, K.V., Wilson, C.J.N., Hobden, B.J., Hammer, J.E., 2010. Diverse patterns of ascent, degassing, and eruption of rhyolite magma during the 1.8 ka Taupo eruption, New Zealand: insights from clast vesicularity. J. Volcanol. Geotherm. Res. 195 (1):31–47. http://dx.doi.org/10.1016/j.jvolgeores.2010.06.002.

Jordan, N., Branney, M., Williams, R., Norry, M., 2013. Stratigraphy and eruption history of pre-Green Tuff peralkaline welded ignimbrites, Pantelleria, Italy. EGU Gen. Assem. Conf. Abstr. vol. 15, p. 2333.

Klug, C., Cashman, K.V., 1994. Vesiculation of May 18, 1980, Mount St. Helens magma. Geology 22 (5):468–472. http://dx.doi.org/10.1130/0091-7613(1994)022.

Klug, C., Cashman, K.V., Bacon, C.R., 2002. Structure and physical characteristics of pumice from the climactic eruption of Mount Mazama (Crater Lake), Oregon. Bull. Volcanol. 64 (7):486–501. http://dx.doi.org/10.1007/s00445-002-0230-5.

Landi, P., Rotolo, S.G., 2015. Cooling and crystallization recorded in trachytic enclaves hosted in pantelleritic magmas (Pantelleria, Italy): implications for pantellerite petrogenesis. J. Volcanol. Geotherm. Res. 301:169–179. http://dx.doi.org/10.1016/j.jvolgeores.2015.05.017.

Landi, P., Metrich, N., Bertagnini, A., Rosi, M., 2004. Dynamics of magma mixing and degassing recorded in plagioclase at Stromboli (Aeolian Archipelago, Italy). Contrib. Mineral. Petrol. 147 (2):213–227. http://dx.doi.org/10.1007/s00410-004-0555-5.

Lange, R.A., 1997. A revised model for the density and thermal expansivity of K₂O-Na₂O-CaO-MgO-Al₂O₃-SiO₂ liquids from 700 to 1900 K: extension to crustal magmatic temperatures. Contrib. Mineral. Petrol. 130 (1):1–11. http://dx.doi.org/10.1007/s004100050345.

Lange, R.L., Carmichael, I.S.E., 1990. Thermodynamic properties of silicate liquids with emphasis on density, thermal expansion and compressibility. Rev. Mineral. Geochem. 24 (1), 25–64.

Lautze, N.C., Houghton, B.F., 2005. Physical mingling of magma and complex eruption dynamics in the shallow conduit at Stromboli volcano, Italy. Geology 33 (5):425. http://dx.doi.org/10.1130/G21325.1.

Lautze, N.C., Houghton, B.F., 2006. Linking variable explosion style and magma textures during 2002 at Stromboli volcano. Italy. Bull. Volcanol. 69 (4):445–460. http://dx.doi.org/10.1007/s00445-006-0086-1.

Lautze, N.C., Houghton, B.F., 2007. Linking variable explosion style and magma textures during 2002 at Stromboli volcano, Italy. Bull. Volcanol. 69 (4):445–460. http://dx.doi.org/10.1007/s00445-006-0086-1.

Lautze, N.C., Houghton, B.F., 2008. Single explosions at Stromboli in 2002: use of clast microtextures to map physical diversity across a fragmentation zone. J. Volcanol. Geotherm. Res. 170 (3–4):262–268. http://dx.doi.org/10.1016/j.jvolgeores.2007.10.011.

Leduc, L., Gurioli, L., Harris, A., Colò, L., Rose-Koga, E.F., 2015. Types and mechanisms of strombolian explosions: characterization of a gas-dominated explosion at Stromboli. Bull. Volcanol. 77:8. http://dx.doi.org/10.1007/s00445-014-0888-5.

Lin, Q., Neethling, S.J., Dobson, K.J., Courtois, L., Lee, P.D., 2015. Quantifying and minimising systematic and random errors in X-ray micro-tomography based volume measurements. Comput. Geosci. 77:1–7. http://dx.doi.org/10.1016/j.cageo.2014.12.008.

Macdonald, G., Davies, G.R., Bliss, C.M., Leat, P.T., Bailey, D.K., Smith, R.L., 1987. Geochemistry of high-silica peralkaline rhyolites, Naivasha, Kenya Rift Valley. J. Petrol. 28 (6), 979–1008.

Mader, H.M., Llewellin, E.W., Mueller, S.P., 2013. The rheology of two-phase magmas: a review and analysis. J. Volcanol. Geotherm. Res. 257:135–158. http://dx.doi.org/10.1016/j.jvolgeores.2013.02.014.

Mahood, G.A., 1984. Pyroclastic rocks and calderas associated with strongly peralkaline magmatism. J. Geophys. Res. 89 (B10):8540–8552. http://dx.doi.org/10.1029/JB089iB10p08540.

Mahood, G.A., Hildreth, W., 1986. Geology of the peralkaline volcano at Pantelleria, Strait of Sicily. Bull. Volcanol. 48 (2):143–172. http://dx.doi.org/10.1007/BF01046548.

Mangan, M.T., Cashman, K.V., 1996. The structure of basaltic scoria and reticulite and inferences for vesiculation, foam formation, and fragmentation in lava fountains. J. Volcanol. Geotherm. Res. 73 (1–2):1–18. http://dx.doi.org/10.1016/0377-0273(96)00018-2.

Mangan, M.T., Cashman, K.V., Newman, S., 1993. Vesiculation of basaltic magma during eruption. Geology 21 (2):157–160. http://dx.doi.org/10.1130/0091-7613(1993)021.

Metrich, N., Bertagnini, A., Landi, P., Rosi, M., 2001. Crystallization driven by decompression and water loss at Stromboli Volcano (Aeolian Islands, Italy). J. Petrol. 42 (8): 1471–1490. http://dx.doi.org/10.1093/petrology/42.8.1471.

Mueller, S., Scheu, B., Spieler, O., Dingwell, D.B., 2008. Permeability control on magma fragmentation. Geology 36 (5):399. http://dx.doi.org/10.1130/G24605A.1.

Namiki, A., Manga, M., 2008. Transition between fragmentation and permeable outgassing of low viscosity magmas. J. Volcanol. Geotherm. Res. 169 (1–2), 48–60.

Neave, D.A., Fabbro, G., Herd, R.A., Petrone, C.M., Edmonds, M., 2012. Melting, differentiation and degassing at the Pantelleria Volcano, Italy. J. Petrol. 53 (3):637–663. http://dx.doi.org/10.1093/petrology/egr074.

Ochs, F.A., Lange, R.A., 1999. The density of hydrous magmatic liquids. Science 283 (5406):1314–1317. http://dx.doi.org/10.1126/science.283.5406.1314.

Orsi, G., Ruvo, L., Scarpati, C., 1989. The Serra della Fastuca Tephra at Pantelleria: physical parameters for an explosive eruption of peralkaline magma. J. Volcanol. Geotherm. Res. 39 (1):55–60. http://dx.doi.org/10.1016/0377-0273(89)90020-6.

Orsi, G., Ruvo, L., Scarpati, C., 1991. The recent explosive volcanism at Pantelleria. Geol. Rundsch. 80 (1):187–200. http://dx.doi.org/10.1007/BF01828776.

Papale, P., 1999. Strain-induced magma fragmentation in explosive eruptions. Nature 397:425–428. http://dx.doi.org/10.1038/17109.

Papale, P., Moretti, R., Barbato, D., 2006. The compositional dependence of the saturation surface of H₂O + CO₂ fluids in silicate melts. Chem. Geol. 229 (1–3):78–95. http://dx.doi.org/10.1016/j.chemgeo.2006.01.013.

Polacci, M., Pioli, L., Rosi, M., 2003. The Plinian phase of the Campanian Ignimbrite eruption (Phlegrean Fields, Italy): evidence from density measurements and textural characterization of pumice. Bull. Volcanol. 65 (6):418–432. http://dx.doi.org/10.1007/s00445-002-0268-4.

Polacci, M., Baker, D.R., Mancini, L., Favretto, S., Hill, R.J., 2009. Vesiculation in magmas from Stromboli and implications for normal Strombolian activity and paroxysmal explosions in basaltic systems. J. Geophys. Res. 114:B01206. http://dx.doi.org/10.1029/2008JB005672.

Rotella, M.D., Wilson, C.J.N., Barker, S.J., Cashman, K.V., Houghton, B.F., Wright, I.C., 2014. Bubble development in explosive silicic eruptions: insights from pyroclast vesicularity textures from Raoul volcano (Kermadec arc). Bull. Volcanol. 76:826. http://dx.doi.org/10.1007/s00445-014-0826-6.

Rotolo, S.G., La Felice, S., Mangakaviti, A., Landi, P., 2007. Geology and petrochemistry of the recent (<25 ka) silicic volcanism at Pantelleria Island. Boll. Soc. Geol. Ital. 126, 191–208.

Rotolo, S.G., Scaillet, S., La Felice, S., Vita-Scaillet, G., 2013. A revision of the structure and stratigraphy of pre-Green Tuff ignimbrites at Pantelleria (Strait of Sicily). J. Volcanol. Geotherm. Res. 250:61–74. http://dx.doi.org/10.1016/j.jvolgeores.2012.10.009.

Rust, A.C., Manga, M., 2002. Effects of bubble deformation on the viscosity of dilute suspensions. J. Non-newton. Fluid Mech. 104 (1):53–63. http://dx.doi.org/10.1016/S0377-0257(02)00013-7.

Rutherford, M.J., Sigurdsson, H., Carey, S., Davis, A., 1985. The May 18, 1980, eruption of Mount St. Helens: 1. Melt composition and experimental phase equilibria. J. Geophys. Res. 90 (B4):2929–2947. http://dx.doi.org/10.1029/JB090iB04p02929.

Sable, J.E., Houghton, B.F., Wilson, C.J.N., Carey, R.J., 2006. Complex proximal sedimentation from Plinian plumes: the example of Tarawera 1886. Bull. Volcanol. 69: 89–103. http://dx.doi.org/10.1007/s00445-006-0057-6.

Sable, J.E., Houghton, B.F., Wilson, C.J.N., Carey, R.J., 2009. Eruption mechanisms during the climax of the Tarawera 1886 basaltic Plinian eruption inferred from microtextural characteristics of the deposits. In: Self, S., Larsen, J., Rowland, K., Hoskuldsson, A., Thordason, T. (Eds.), Studies in Volcanology: The Legacy of George Walker. Geol. Soc, London.

Sahagian, D.L., Proussevitch, A.A., 1998. 3D particle size distributions from 2D observations: stereology for natural applications. J. Volcanol. Geotherm. Res. 84 (3–4): 173–196. http://dx.doi.org/10.1016/S0377-0273(98)00043-2.

Scaillet, S., Vita-Scaillet, G., Rotolo, S.G., 2013. Millennial-scale phase relationships between ice-core and Mediterranean marine records: insights from high-precision ⁴⁰Ar/³⁹Ar dating of the Green Tuff of Pantelleria, Sicily Strait. Quat. Sci. Rev. 78: 141–154. http://dx.doi.org/10.1016/j.quascirev.2013.08.008.

Schmincke, H.-U., 1974. Volcanological aspects of peralkaline silicic welded ash-flow tuffs. Bull. Volcanol. 38 (2):594–636. http://dx.doi.org/10.1007/BF02596900.

Shea, T., Houghton, B.F., Gurioli, L., Cashman, K.V., Hammer, J.E., Hobden, B.J., 2010. Textural studies of vesicles in volcanic rocks: an integrated methodology. J. Volcanol. Geotherm. Res. 190 (3–4):271–289. http://dx.doi.org/10.1016/j.jvolgeores.2009.12.003.

Shea, T., Gurioli, L., Houghton, B.F., 2012. Transitions between fall phases and pyroclastic density currents during the AD 79 eruption at Vesuvius: building a transient conduit model from the textural and volatile record. Bull. Volcanol. 74 (10), 2363–2381.

Shea, T., Hellebrand, E., Gurioli, L., Tuffen, H., 2014. Conduit to localized-scale degassing during plinian eruptions: insights from major element and volatile (Cl and H₂O) analyses within Vesuvius AD 79 pumice. J. Petrol. 55 (2), 315–344.

Sigurdsson, H., Sparks, R.S.J., 1981. Petrology of rhyolitic and mixed magma ejecta from the 1875 eruption of Askja, Iceland. J. Petrol. 22 (1):41–84. http://dx.doi.org/10.1093/petrology/22.1.41.

Sparks, R.S.J., 1978. The dynamics of bubble formation and growth in magmas: a review and analysis. J. Volcanol. Geotherm. Res. 3 (1–2):1–37. http://dx.doi.org/10.1016/0377-0273(78)90002-1.

Spieler, O., Kennedy, B., Kueppers, U., Dingwell, D.B., Scheu, B., Taddeucci, J., 2004. The fragmentation threshold of pyroclastic rocks. Earth Planet. Sci. Lett. 226 (1–2): 139–148. http://dx.doi.org/10.1016/j.epsl.2004.07.016.

Stevenson, R.J., Wilson, L., 1997. Physical volcanology and eruption dynamics of peralkaline agglutinates from Pantelleria. J. Volcanol. Geotherm. Res. 79 (1–2): 97–122. http://dx.doi.org/10.1016/S0377-0273(97)00021-8.

Sutton, A.N., Blake, S., Wilson, C.J.N., 1995. An outline geochemistry of rhyolite eruptives from Taupo volcanic Centre, New Zealand. J. Volcanol. Geotherm. Res. 68 (1–3): 153–175. http://dx.doi.org/10.1016/0377-0273(95)00011-I.

Toplis, M.J., Dingwell, D.B., Libourel, G., 1994. The effect of phosphorus on the iron redox ratio, viscosity, and density of an evolved ferro-basalt. Contrib. Mineral. Petrol. 117 (3):293–304. http://dx.doi.org/10.1007/BF00310870.

Toramaru, A., 2006. BND (bubble number density) decompression rate meter for explosive volcanic eruptions. J. Volcanol. Geotherm. Res. 154 (3–4):303–316. http://dx. doi.org/10.1016/j.jvolgeores.2006.03.027.

Villari, L., 1974. The island of Pantelleria. Bull. Volcanol. 38 (2):680–724. http://dx.doi.org/10.1007/BF02596904.

Vona, A., Romano, C., Dingwell, D.B., Giordano, D., 2011. The rheology of crystal-bearing basaltic magmas from Stromboli and Etna. Geochim. Cosmochim. Acta 75 (11): 3214–3236. http://dx.doi.org/10.1016/j.gca.2011.03.031.

White, J.C., Parker, D.F., Ren, M., 2009. The origin of trachyte and pantellerite from Pantelleria, Italy: insights from major element, trace element, and thermodynamic modelling. J. Volcanol. Geotherm. Res. 179 (1–2):33–55. http://dx.doi.org/10.1016/j.jvolgeores.2008.10.007.

Williams, R., Branney, M.J., Barry, T.L., 2013. Temporal and spatial evolution of a waxing then waning catastrophic density current revealed by chemical mapping. Geology 42 (2):107–110. http://dx.doi.org/10.1130/G34830.1.

Wolff, J.A., Wright, J.V., 1981. Rheomorphism of welded tuffs. J. Volcanol. Geotherm. Res. 10 (1–3):13–34. http://dx.doi.org/10.1016/0377-0273(81)90052-4.

Wright, H.M.N., Weinberg, R.F., 2009. Strain localization in vesicular magma: implications for rheology and fragmentation. Geology 37 (11):1023–1026. http://dx.doi.org/10.1130/G30199A.1.

Zhang, Y., 1999. A criterion for the fragmentation of bubbly magma based on brittle failure theory. Nature 402:648–650. http://dx.doi.org/10.1038/45210.